Supporting Information for

Interfacial Interaction of Ag-MnO_x Heterostructure for Efficient CO_2 Electroreduction to CO and Aqueous Zn-CO_2 Batteries

Chao Wen[a,b], Ziyin Xie[a], Na Wu[a], Lihui Dong[a,b], Bin Li[a,b*], Zhengjun Chen[a*]

[a]Guangxi Key Laboratory of Electrochemical Energy Materials, School of Chemistry and Chemical Engineering, Guangxi University, Nanning 530004, PR China
[b]State Key Laboratory of Featured Metal Materials and Life-cycle Safety for Composite Structures, Guangxi University, Nanning 530004, PR. China

Corresponding Authors
*E-mail addresses: binli@gxu.edu.cn (B. Li); zjchen@gxu.edu.cn (Z. Chen).

Experimental section

2.3 Characterizations

The phase structure was recorded by X-ray diffraction (XRD, BRUKER D8 Discover, Cu Kα radiation) operating at 20 mA and 40 KV. SEM images were obtained by Field-emission scanning electron microscope (FE-SEM, Thermo Fisher Scientific FEI Quattro S) at 5 KV. The morphology and elemental composition were performed utilizing a transmission electron microscope (TEM, FEI Talos F200S) operated at 200 KV. Raman microscope (Renishaw, Horiba HR Evolution-800) and X-ray photoelectron spectrometer (XPS, Thermo Scientific ESCALAB 250Xi) were used to detected the internal structure and chemical state of synthesized samples. The CO_2 Temperature programmed desorption (CO_2 TPD) experiments were performed by an automatic adsorption device (VDSorb-91i, China) to detect the adsorption/desorption of CO_2. The reaction intermediates were analyzed by the attenuated total reflectance surface enhanced infrared absorption spectroscopy (ATR-SEIRAS, Nicolet iS10).

2.4 Electrochemical Measurements

The CO_2RR experiments were conducted out in an H-type air-tight electrolytic cell fitted with an electrochemical workstation (CHI 660E, CH Instruments, Chenhua Co.) and a proton exchange membrane. Ag/AgCl is the reference electrode and the platinum sheet is the counter electrode. The cathode chamber was saturated with CO_2 (99.999% purity) gas for 30 min, and the flow rate was set to 20 sccm with a mass flow controller (Alicat Scientific, LK2) to maintain the CO_2 flux during the experiment. In the preparation of the working electrode, 10 mg of catalyst was sonicated in a mixture of 600 μl of DI water, 360 μl of ethanol and 40 μl of 5.0 wt. % Nafion for 60 minutes to create a uniform ink. Next, 100 μL of the formed ink was coated onto carbon paper (1 × 0.5×2 cm^2) and dried at 60 °C, with a loading of ~ 1.0 $mg \cdot cm^{-2}$. All potentials were not IR-compensated and were converted to the RHE potential according to:

$$E\,(\text{vs. RHE}) = E\,(\text{vs. Ag/AgCl}) + 0.059 \times pH + 0.197$$

Linear scanning voltammetric (LSV) curves were performed on N_2- and CO_2

saturated 0.5 M $KHCO_3$ electrolytes at a scan rate of 10 mV s^{-1}. The carbon monoxide partial current density is based on the following equation: $j_{CO} = j * FE_{CO}$, wherein j_{CO} represents the partial current density for carbon monoxide, j denotes the total current density, FE_{CO} is the Faraday efficiency of carbon monoxide. The linear portion of the plot of overpotential vs the logarithm of the CO bias current density was fitted to produce Tafel slopes. The electrochemical impedance spectra (EIS) were collected at open circuit potential over a frequency range of 10^5 Hz to 10 Hz. Cyclic voltammetry (CV) measurements were conducted at varying scan rates (20, 40, 60, 80, 100 mV s^{-1}) to determine the double-layer capacitance (C_{dl}) and assess the electrochemically active surface area (ECSA) of the catalysts, with the equation:

$$ECSA = C_{dl} / C_s$$

Wherein C_s denotes the specific capacitance.

2.5 Product Analysis

With a thermal conductivity detector (TCD) and a flame ionization detector (FID), the gas chromatography (GC, FULI, GC-9790II) was employed to on-line analysis the cathode gas products in the electrolytic cell. The standard gas was diluted into different concentrations to create a standard curve to analyze the content of different gas products. The following formula was used to determine the FE of the reduced product:

$$FE\ (\%) = \frac{n\,N\,F}{Q_{total}}$$

Where, n represents the amount of substance in moles, and N (= 2) denotes the number of electrons transferred during the electroreduction of carbon dioxide; F (96500 C mol^{-1}) is the Faradaic constant, and Q_{total} is the total charge that flows through the electrodes during the electrolysis process.

2.6 DFT Calculation

All the Density Functional Theory (DFT)[1] calculations were performed using Vienna Ab initio Simulation Package (VASP)[2] with the projector augmented wave (PAW)[3] method. The Perdew-Burke-Ernzerhof (PBE)[4] of parameterization of the generalized gradient approximation (GGA)[5] is adopted to describe the exchange and correlation potential. During the geometry optimization and electronic structure calculations, the cut-off energy of plane-wave basis set is 400 eV, and single gamma-point grid sampling was used for Brillouin zone integration. Atomic positions were optimized until the forces were less than 0.05 eV/Å. The first Brillouin zone was sampled by 1 × 1 × 1 k-mesh and a vacuum thickness of about 15 Å between periodic images was adopted, which were found to be sufficient for accurate results. Grimme's method (DFT-D3)[6] was carried out to include explicit dispersion correction terms to the energy. The simulated Ag(111) surface contains 4 atomic-layers (100 atoms) and a vacuum layer (~ 15 Å). The manganese oxide clusters were subsequently placed on the Ag surface to obtain the MnO_x/Ag (111) structure. During geometries optimization, the atoms in bottom 2 layers were fixed, and other atoms were fully relaxed until the force on each atom were less than 0.05 eV/Å. The Gibbs Free Energy (ΔG) are calculated using:

$$\Delta G = \Delta E + \Delta ZPE - T\Delta S$$

where ΔE, ΔZPE, and TΔS are the adsorption energy of intermediates, Zero-Point-Energy, and en-tropy correction under reaction temperature (298.15 K).

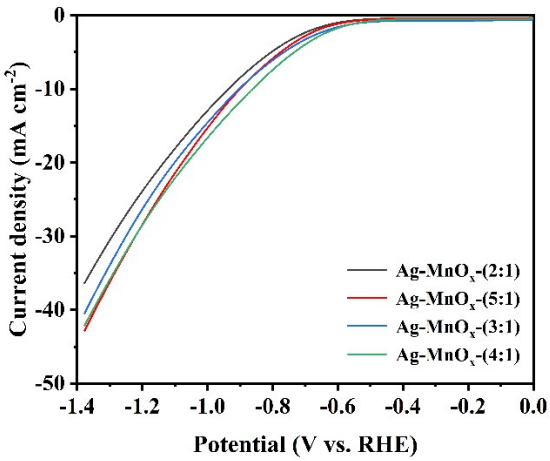

Fig. S1. The LSV curves of catalysts with various Ag/Mn feeding ratios

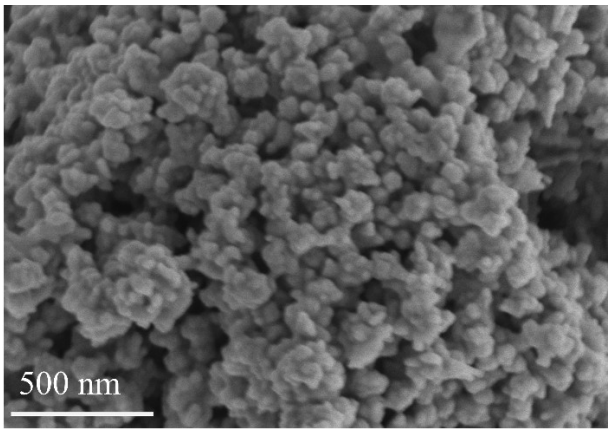

Fig. S2. SEM image of the comparative Ag sample

Table S1 The surface fraction of Mn elements by XPS spectra.

(%) / catalyst	Mn 2p$_{3/2}$			
	Mn^{4+}	Mn^{3+}	Mn^{2+}	$(Mn^{3+}+Mn^{2+})/Mn^{4+}$
MnO_x	45.8	36.5	17.7	118.1
Ag-MnO_x	34.4	49.2	16.4	190.9

Table S2 The surface fraction of O elements by XPS spectra

(%) catalyst	O 1s		
	O_{sur}	O_{vac}	O_{lat}
MnO_x	11.9	39.9	48.2
Ag-MnO_x	16.4	43.4	40.2

Table S3 Summary of silver-based catalyst performance in recent years

Catalyst	FE_{CO}	j_{CO} (mA cm^{-2})	Electrode configuration	electrolytes
Ag_1/MnO_2 SAC[7]	95.7%	3.4 at -0.9 V	H-type cell	0.5 M $KHCO_3$
Ag-N_x[8]	95%	2.5 at -0.377 V	H-type cell	0.1 M $KHCO_3$
Cu/Ag (S)[9]	93%	2.9 at -1.0 V	H-type cell	0.1 M $KHCO_3$
Ag-In $(OH)_3$[10]	93%	0.6 at -0.7 V	H-type cell	0.5 M $KHCO_3$
Tri-Ag-NPs[11]	96.8%	1.25 at -0.856 V	H-type cell	0.1 M $KHCO_3$
Ag-BTC[12]	95%	7.2 at -1.0 V	H-type cell	0.1 M $KHCO_3$
PON-Ag[13]	96.7%	4.4 at -0.69 V	H-type cell	0.5 M $KHCO_3$
Porous Ag[14]	96.38%	5.3 at -0.8 V	H-type cell	0.5 M $KHCO_3$
Ag-Cu aerogel[15]	89.40%	5.86 at -0.89 V	H-type cell	0.1 M $KHCO_3$
Ag layer-Zn[16]	84.2%	2.97 at −1.0 V	H-type cell	0.1 M $KHCO_3$
Cu-Ag biphasic[17]	80.25%	4.88 at − 0.9 V	H-type cell	0.1 M $KHCO_3$
Ag-MnO_x (this work)	97.5%	7.05 at -0.8 V	H-type cell	0.5 M $KHCO_3$

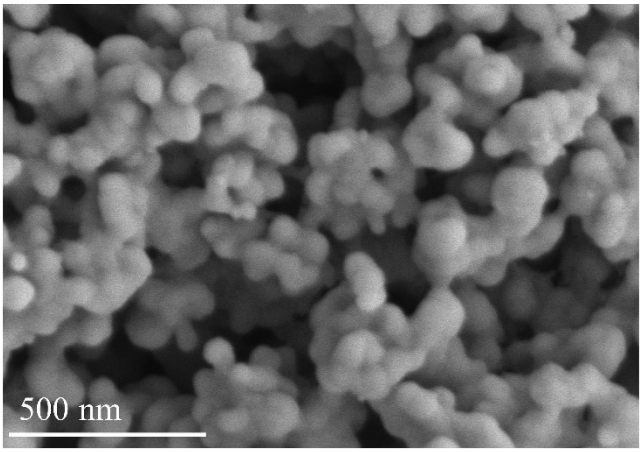

Fig. S3. SEM image of Ag-MnO_x after stability testing

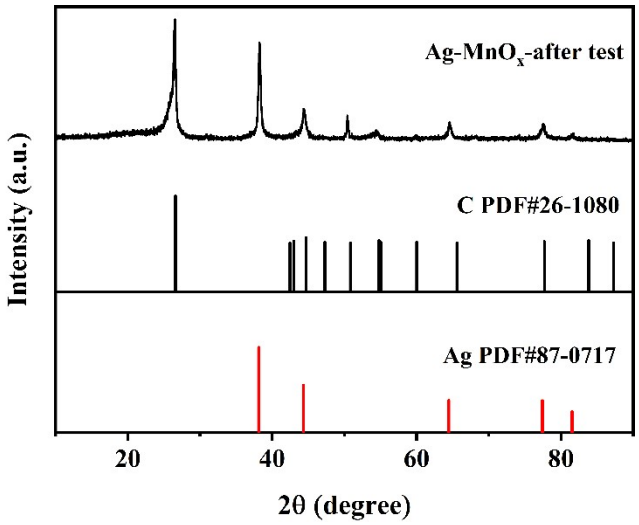

Fig. S4. XRD pattern of Ag-MnO$_x$ after stability testing

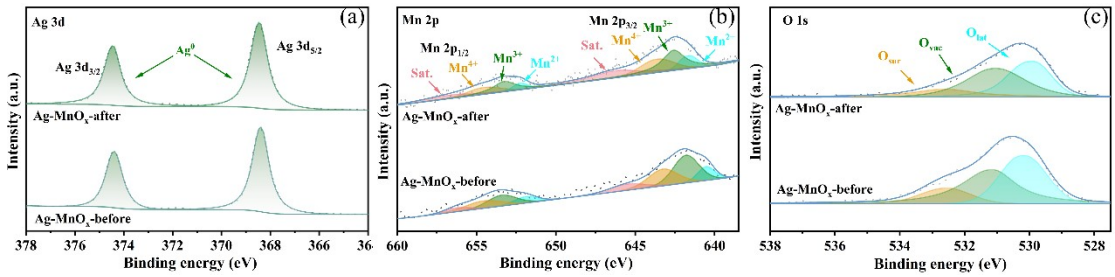

Fig. S5. Ag 3d, b) Mn 2p, c) O 1s XPS spectra of the Ag-MnO$_x$ sample before and after stability testing

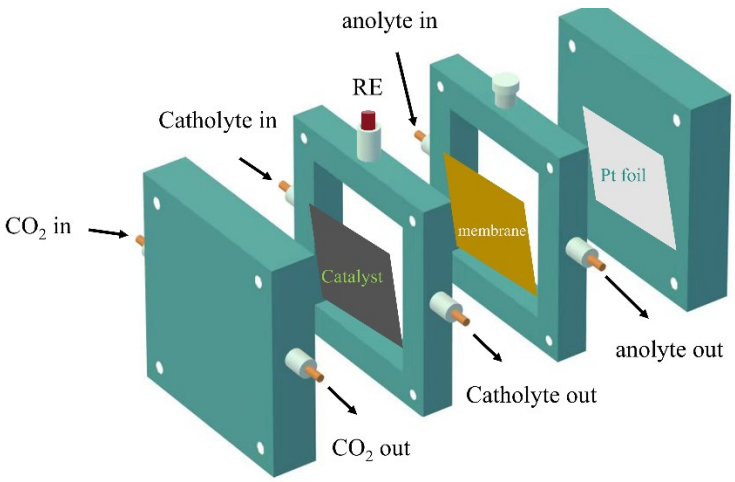

Fig. S6. Flow cell (where, RE is reference electrode.)

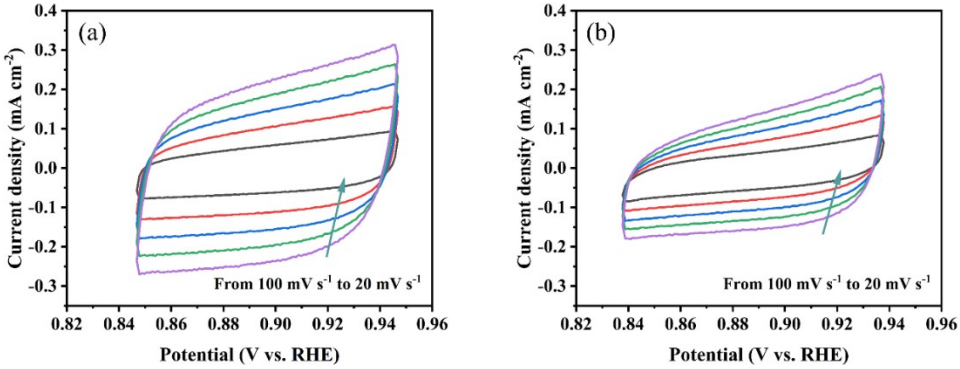

Fig. S7. a) CV of Ag-MnO_x. b) CV of Ag

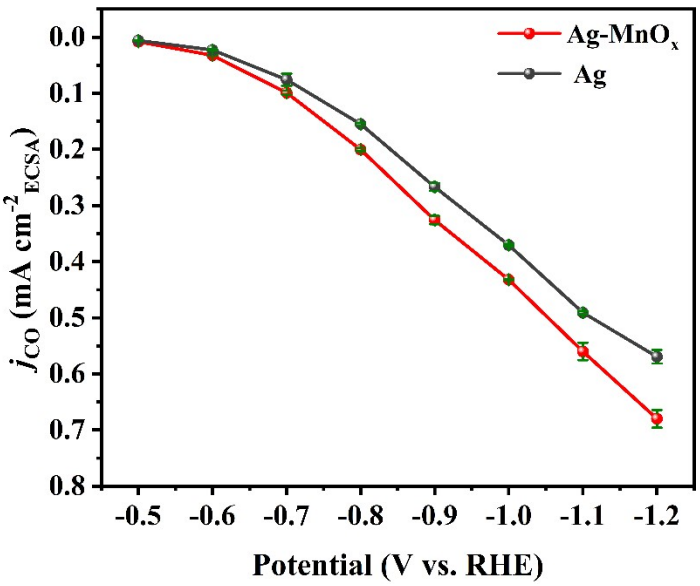

Fig. S8. The ECSA normalized j_{CO} of Ag-MnO_x and Ag

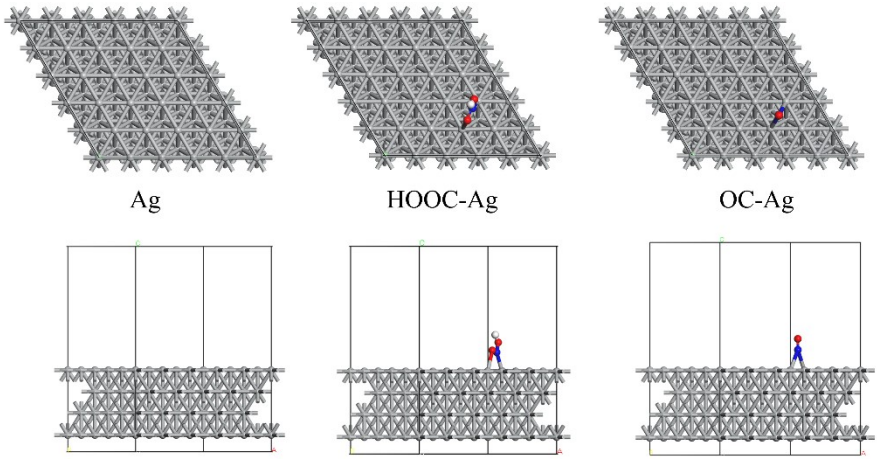

Fig. S9. Optimized structure of Ag, HOOC-Ag and OC-Ag. Silver gray, red, white, and blue spheres represent the Ag, O, H, and C atoms, respectively.

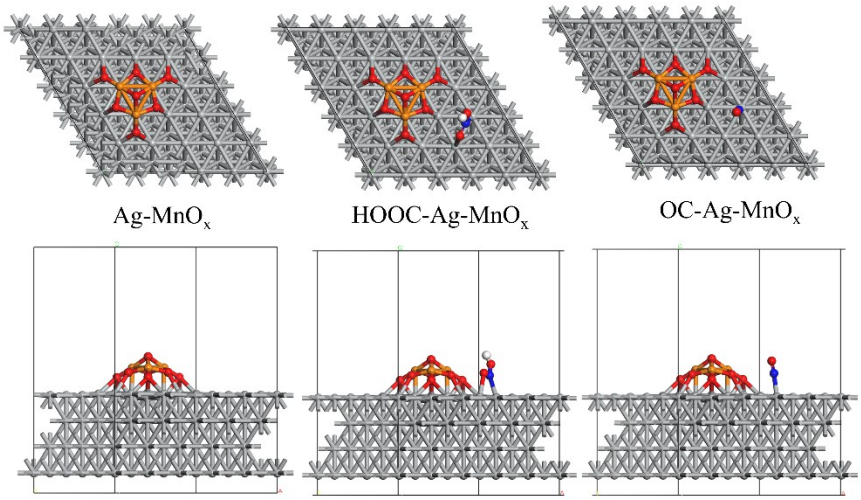

Fig. S10. Optimized structure of Ag-MnO$_x$, HOOC- Ag-MnO$_x$ and OC- Ag-MnO$_x$. Silver gray, red, orange, white, and blue spheres represent the Ag, O, Mn, H, and C atoms, respectively.

Reference

1 X. Liao, R. Lu, L. Xia, Q. Liu, H. Wang, K. Zhao, Z. Wang and Y. Zhao, Density functional theory for electrocatalysis, *Energy Environ. Mater.* , 2021, **5**, 157-185.

2 J. F. G. Kresse, Efficiency of ab-initio total energy calculations for metals and semiconductors using a

plane-wave basis set, *Comp. Mater. Sci.* , 1996, **6**, 15-50.

3 S. Kang, S. Ryu, S. Choi, J. Kim, K. Hong and W. Y. Kim, Update to ACE-molecule: projector augmented wave method on lagrange-sinc basis set, *Int. J. Quantum Chem.*, 2016, **116**, 644-650.

4 R. M. Irelan, T. M. Henderson and G. E. Scuseria, Long-range-corrected hybrids using a range-separated Perdew-Burke-Ernzerhof functional and random phase approximation correlation, *J. Chem. Phys.*, 2011, **135**, 094105.

5 A. Albavera-Mata, K. Botello-Mancilla, S. B. Trickey, J. L. Gázquez and A. Vela, Generalized gradient approximations with local parameters, *Phys. Rev. B* 2020, **102**, 035129.

6 H. Schröder, J. Hühnert and T. Schwabe, Evaluation of DFT-D3 dispersion corrections for various structural benchmark sets, *J. Chem. Phys.*, 2017, **146**, 044115.

7 N. Zhang, X. Zhang, L. Tao, P. Jiang, C. Ye, R. Lin, Z. Huang, A. Li, D. Pang, H. Yan, Y. Wang, P. Xu, S. An, Q. Zhang, L. Liu, S. Du, X. Han, D. Wang and Y. Li, Silver single-atom catalyst for efficient electrochemical CO_2 reduction synthesized from thermal transformation and surface reconstruction, *Angew. Chem., Int. Ed.*, 2021, **60**, 6170-6176.

8 R. Sui, J. Pei, J. Fang, X. Zhang, Y. Zhang, F. Wei, W. Chen, Z. Hu, S. Hu, W. Zhu and Z. Zhuang, Engineering Ag–N_x single-atom sites on porous concave N-doped carbon for boosting CO_2 electroreduction, *ACS Appl. Mater. Interfaces*, 2021, **13**, 17736-17744.

9 Z. Ma, T. Wan, D. Zhang, J. A. Yuwono, C. Tsounis, J. Jiang, Y.-H. Chou, X. Lu, P. V. Kumar, Y. H. Ng, D. Chu, C. Y. Toe, Z. Han and R. Amal, Atomically dispersed Cu catalysts on sulfide-derived defective Ag nanowires for electrochemical CO_2 reduction, *ACS Nano*, 2023, **17**, 2387-2398.

10 L. Fu, Z. Qu, L. Zhou and Y. Ding, Boosting electrochemical CO_2 reduction to CO over interfacial hydroxide-metal catalysts, *Appl. Catal., B*, 2023, **339**, 123170.

11 S. Liu, H. Tao, L. Zeng, Q. Liu, Z. Xu, Q. Liu and J.-L. Luo, Shape-dependent electrocatalytic reduction of CO_2 to CO on triangular silver nanoplates, *J. Am. Chem. Soc.*, 2017, **139**, 2160-2163.

12 W. T. Yu, S. Z. Chen, J. Y. Zhu, Z. Q. He and S. Song, A highly dispersed and surface-active Ag-BTC catalyst with state-of-the-art selectivity in CO_2 electroreduction towards CO, *J CO2 Util*, 2023, **70**, 102457.

13 X. Peng, S. G. Karakalos and W. E. Mustain, Preferentially oriented Ag nanocrystals with extremely high activity and faradaic efficiency for CO_2 electrochemical reduction to CO, *ACS Appl. Mater. Interfaces*, 2018, **10**, 1734-1742.

14 W. Guo, K. Shim, F. O. Odongo Ngome, Y. H. Moon, S.-Y. Choi and Y.-T. Kim, Highly active coral-like porous silver for electrochemical reduction of CO_2 to CO, *J CO2 Util*, 2020, **41**, 101242.

15 W. Wang, S. Gong, J. Liu, Y. Ge, J. Wang and X. Lv, Ag-Cu aerogel for electrochemical CO_2 conversion to CO, *J. Colloid Interface Sci.* , 2021, **595**, 159-167.

16 W. Guo, K. Shim and Y. T. Kim, Ag layer deposited on Zn by physical vapor deposition with enhanced CO selectivity for electrochemical CO_2 reduction, *Appl. Surf. Sci.*, 2020, **526**, 146651.

17 T. Zhang, Y. Liu, C. Yang, L. Tian, Y. Yan and G. Wang, Monotonically increasing relationship between conversion selectivity from CO_2 to CO and the interface area of Cu-Ag biphasic electrochemical catalyst, *J. Alloys Compd.*, 2023, **947**, 169638.